

Probabilistic Tracking with Deep Factors

Fan Jiang Andrew Marmon
Ildebrando De Courten Frank Dellaert
Georgia Institute of Technology
Atlanta, GA

{fan.jiang|amarmon3|icourten3|fd27}@gatech.edu

Marc Rasi

Google Brain
Mountain View, CA

marcrasi@google.com

Abstract

In many applications of computer vision it is important to accurately estimate the trajectory of an object over time by fusing data from a number of sources, of which 2D and 3D imagery is only one. In this paper, we show how to use a deep feature encoding in conjunction with generative densities over the features in a factor-graph based, probabilistic tracking framework. We present a likelihood model that combines a learned feature encoder with generative densities over them, both trained in a supervised manner. We also experiment with directly inferring probability through the use of image classification models that feed into the likelihood formulation. These models are used to implement deep factors that are added to the factor graph to complement other factors that represent domain-specific knowledge such as motion models and/or other prior information. Factors are then optimized together in a non-linear least-squares tracking framework that takes the form of an Extended Kalman Smoother with a Gaussian prior. A key feature of our likelihood model is that it leverages the Lie group properties of the tracked target’s pose to apply the feature encoding on an image patch, extracted through a differentiable warp function inspired by spatial transformer networks. To illustrate the proposed approach we evaluate it on a challenging social insect behavior dataset, and show that using deep features does outperform these earlier linear appearance models used in this setting.

1. Introduction

In many applications of computer vision it is important to accurately estimate the trajectory of an object over time by fusing data from a number of sources, of which imagery is only one. For example, when tracking a person from an autonomous vehicle, the known ego-motion of the vehicle and probabilistic motion models of the person can be brought to bear [23]. This holds as well for tracking other vehicles, for which we might have even more accurate mo-

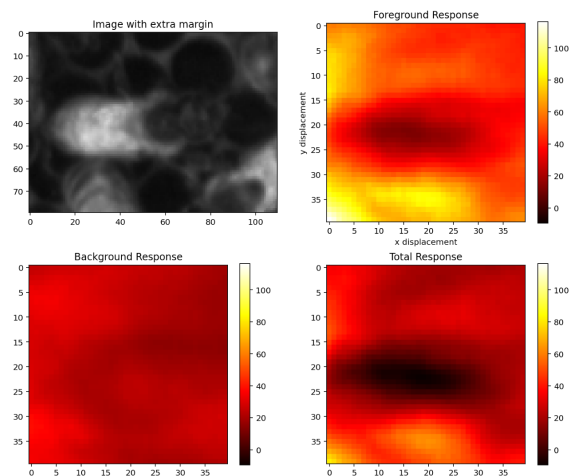


Figure 1. Our proposed deep factor log-likelihood is illustrated here for a bee-tracking example. In this case, the decode stage of an auto-encoder induces a negative log-likelihood $\phi_F(\delta_x, \delta_y)$ and $\phi_B(\delta_x, \delta_y)$ for respectively the foreground and background class, here shown just for translation, although the pose g is an element of $SE(2)$. The total response is $\phi_F(\delta_x, \delta_y) - \phi_B(\delta_x, \delta_y)$.

tion information. Finally, and this is the application we will focus on in this paper, when tracking animals or social insects, behavior models might be available that constrain and help recover the actual movements.

Thanks to recent advances in tracking that make use of deep learning, the usability of tracking in real world scenarios has been greatly improved. Two representative examples are Transformer Tracking [9] and RPT [31], both showing impressive performance.

However, modern tracking methods usually do not deal with other sources of information and rarely learn or use a motion model [32]. Some recent work [8, 52] implicitly model object motion implicitly in the form of a recurrent network, which helps ambiguity resolution in the presence of multiple similar objects. In particular, Zhong *et al.* [52] introduce the idea of iterative updating in a coarse-to-fine framework.

In the field of animal tracking, motion models have also been used to assist in dense entity resolution for tracking [5] or to define an Region-Of-Interest (ROI) as input to infer an animal’s pose [33]. These methods however cannot be used to inject probabilistic information about the target, and can certainly not correct for it after *ex post*. Meanwhile, energy-based approaches like ours can be easily combined with other sources of information (See also Fig. 8 in [28]).

In this paper we show how to use deep feature encoding in conjunction with generative models over the features in a probabilistic tracking framework. We use factor graphs, graphical models that have become popular in state estimation [18], navigation [14], and mapping [40] to model the different sources of measurement information and probabilistic prior knowledge. Most factors are designed by hand, however, and only a handful of papers have leveraged data to learn the functions associated with them, see e.g. [11, 38].

A key feature of our likelihood model is that it leverages the Lie group properties of the tracked target’s pose to apply the feature encoding on an image patch, extracted through a differentiable warp function inspired by spatial transformer networks (STNs) [22]. This is similar, but different from the decoupled approach in [10]. We frame this in a general way such that the pose can be any smooth manifold, including but not limited to 2D and 3D rigid transforms or similarity transforms.

While the derivative of a neural network (NN) mapping is usually only used in the incremental update of the NN parameters, there exists literature that successfully exploits the backward pass, most notably, to generating adversarial samples [17] and incremental updating of motion estimates [7]. In our approach, we use the derivative of the neural network to implicitly carry out inference, in the the spirit of Structured Prediction Energy Networks (SPENs) [1].

To illustrate the proposed approach we evaluate it on a challenging social insect application, a domain where previous approaches have already applied generative models [24]. We show using that deep features does outperform these earlier linear appearance models, and show that simple Gaussian generative foreground and background densities suffice to obtain excellent results even when compared with modern complex networks.

2. Related Work

Classical Methods: In recent years, the majority of state of the art object trackers have been based on two dominant methodologies: The discriminative correlation filter [4, 12, 20, 3] and the Siamese correlation network [2, 46, 39, 51]. Both methods compute a similarity metric between a target object’s appearance and proposed image patches over the current frame, albeit with different architectures. A good review on these types of tracking methods can be found in [15]. Our method similarly computes a value for simi-

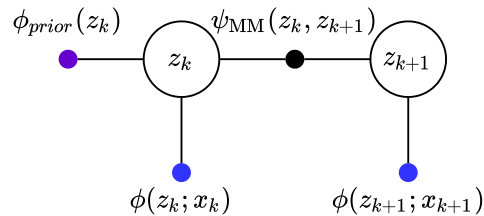


Figure 2. Trajectory optimization factor graph. Purple: Prior Factor; blue: tracking factor; black: between factor.

larity on the proposed image patches and additionally optimises on the best proposed patch. In particular, our method leverages the Lie-Group properties of the target’s pose to compute the similarity metric and to optimize the the patch with gradient descent.

Inverse Compositional (IC) Methods: One notable method in the tracking literature is Deep-LK [45], which also employed an *iterative updating* approach using cascaded linear regression with a deep feature encoder. Their method is further extended by [30] to enable 3D tracking in a SE(3) manifold, whom also introduced learn-able optimization primitives to ease up the assumptions in the original IC formulation. By exploiting the IC method, these approaches can achieve both good accuracy and fast computation speed. However, such a non-probabilistic formulation also denied easy injection of domain specific knowledge into the optimization pipeline.

Energy-based Models: Tracking with our factor graph consists of finding poses and associated appearances that minimize the sum of factors. Our approach inherits from energy-based models which learn an energy function that is low around observed data and is high otherwise [28]. Although not explicitly energy-based, previous tracking methods have utilized Siamese correlation networks effectively to compute a response map over the tracked target’s new position [2, 46, 39, 51]. This output response map does not require the calculation of a normalization constant like other probabilistic models and can be used to directly infer a tracked target’s position to exploit the same advantage that energy-based models do. However, this generated response map is based on the forward pass of a deep learning model and does not easily allow for the addition of sources of information other than appearance. Our approach leverages the backward pass to optimize for an object’s trajectory w.r.t. the energy at an observed pose.

3. Approach

3.1. Energy-based Tracking

We model the state z_k as consisting of a pose $g_k \in G$ and appearance $a_k \in A$, although our approach generalizes to adding more state, e.g., velocities to accommodate

more complex motion models. We assume that G is an n -dimensional Lie group, e.g., $SE(2)$ or $SE(3)$, so that any pose g can be written using the exponential map as $g = \exp(\xi)$ with $\xi \in R^n$ an element of the Lie algebra.

We formulate the problem as a factor graph (Fig. 2), with the hidden states z_k as the unknown variables, and with factors expressing the negative log-likelihood over the combination of variables they are connected to. We then recover the optimal incremental trajectory Z^* as the minimizer of

$$Z^* = \arg \min_Z \sum_i f_i(Z_i), \quad (1)$$

where Z_i is the set of variables connected to factor f_i .

In tracking the factor graph is a simple Markov chain, with binary factors $\psi(z_k, z_{k+1})$ for the motion model, and unary factors $\phi(z_k; x_k)$ modeling the likelihood of the state z_k given frame x_k . A simple way to model the motion is as a simple Brownian motion, using

$$\psi(g_k, g_{k+1}) = \|\log(g_k^{-1}g_{k+1})\|_Q^2 \quad (2)$$

where \log is the inverse of the exponential map, Q is an $n \times n$ covariance matrix, and $\|e\|_Q^2$ denotes the squared Mahalanobis error with covariance Q .

The time evolution of the appearance variables a_k can be modeled via a generic binary factor,

$$\psi(a_k, a_{k+1}) = -\log p(a_{k+1}|a_k), \quad (3)$$

e.g., encoding Markov transition probabilities in the discrete case, or a continuous random walk in the case of continuous variables.

Note here that there is no limit to how many additional data sources could be added to the factor graph. Data sources could include GPS, physical markers [33] or Lidar. Additionally there is no limit to how elaborate the motion could be. Modelling velocity, acceleration and jerk can be done in this tracking framework.

3.2. The Likelihood Model

A key contribution is formulating the unary likelihood model $\phi(z_k; x_k)$ as the likelihood ratio for a region $R(g_k, x_k)$, obtained through a differentiable warp R . In particular, R extracts a patch from a region of interest (oriented bounding box) from the image x_k around pose g_k :

$$\phi(z_k; x_k) = -\log \frac{p_F(C(R(g_k, x_k))|a_k)}{p_B(C(R(g_k, x_k)))} \quad (4)$$

$$= \phi_F(g_k, a_k; x_k) - \phi_B(g_k; x_k). \quad (5)$$

Above p_F is a conventional probabilistic foreground model and p_B is a conventional probabilistic background model, but the mapping C is a data-driven feature encoding from the image region to a d -dimensional feature vector $c \in R^d$.

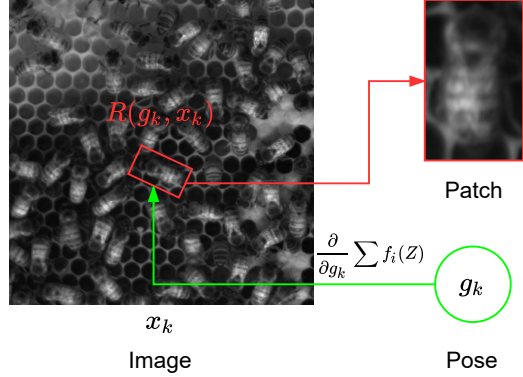


Figure 3. Central to our approach is a differentiable warp R that extracts a region of interest from the image x_k around pose g_k .

The specific form of (4) is informed by [37], in which the authors emphasized the importance of explicitly modeling the background in generative modeling.

In Equation (5) we explicitly write this as a foreground factor ϕ_F and background factor ϕ_B to emphasize the factor graph structure. Because they are obtained by taking the negative log of a probability density, they can be interpreted in an energy minimization framework as illustrated graphically in Figure 1.

The feature encoding $C(\cdot)$ itself can be learned, introducing deep trainable factors into a probabilistic trajectory optimization framework. The three encodings we evaluated are detailed in Section 4.

3.3. Generative Models over the Feature Space

For the foreground model p_F and background model p_B we have used both a full covariance Gaussian model and a naïve Bayes model (a Gaussian model with a diagonal covariance matrix). In either case, we have

$$\phi_{\{F,B\}}(g; x) \doteq -\log p_{\{F,B\}}(c) \quad (6)$$

$$= -\log \mathcal{N}(c; \mu_{\{F,B\}}, \Sigma_{\{F,B\}}), \quad (7)$$

with $c = C(R(g, x))$ and where $\mu_{\{F,B\}}$ and $\Sigma_{\{F,B\}}$ are the mean and covariance matrix for the foreground and background respectively.

Both foreground and background model are trained in a supervised manner on the extracted feature vectors $c = C(R(g, x))$, but for the background model we use arbitrary regions $R(g_{ij}^B, x_i)$ at poses g_{ij}^B in the i^{th} image that have minimal overlap with the foreground regions $R(g_{ij}^F, x_i)$.

3.4. Optimization

Computationally it is infeasible to compute $f_i(Z_i)$ for all possible z_{k+1} states. Therefore, $f_i(Z_i)$ can only be computed for a subset of these possible states. Other tracking papers [46, 29] use a region proposal network to constrain

Algorithm 1 Tracking by Optimization

- 1: $K \leftarrow$ number of video frames
 - 2: **for** k in $1 \dots K$ **do**
 - 3: let $x_k = k$ -th image
 - 4: **for** i in $1 \dots N$ **do**
 - 5: sample pose g_i from motion model $\psi(g_k, g_{k+1})$
 - 6: extract image patch $P_i = R(g_i, x_k)$
 - 7: compute error E from image patch
 - 8: select best sample $g_b = \arg \min_{g_i} (E(g_i))$
 - 9: final pose $g_f = \text{GradientDescent}(g)$
-

the possible target locations. Our method instead uses a motion model $\psi(g_k, g_{k+1})$ to provide initial guesses and then optimises the best guess. As shown in Algorithm 1, N poses are sampled from the motion model and their error values $E(g)$ are computed.

$$E(g) = \psi(g_k, g_{k+1}) + \phi(z_{k+1}; x_{k+1}) \quad (8)$$

As show in equation (8), the error value at a given state z_{k+1} is a sum of the binary motion factor and the unary tracking factor.

Then the pose with the lowest error $E(g)$ is further optimized with gradient descent. This part of the algorithm is one of the main contributions of this paper. The derivative of the error E is taken with respect to the Lie group parameters $(x, y, \theta$ in case of $\text{SE}(2)$) and the pose is moved with respect to those parameters in the direction of steepest descent. This is performed until the pose converges to a local minimum.

4. Feature Encodings

In the results section below we experiment with regularized auto-encoders (RAE, see [16]), probabilistic principal component analysis (PPCA, see [41]), random projections, and Big Transfer [26]. We detail each of these below.

4.1. Regularized Auto-encoders

Regularized Auto-encoders (RAEs) are a recent development in obtaining a principled generative density over a domain, see [16] for more details. In this approach, we first train the auto-encoder backbone with the RAE loss

$$\mathcal{L}_{\text{RAE}} = \mathcal{L}_{\text{REC}} + \mathcal{L}_{\text{C}}^{\text{RAE}} + \lambda \mathcal{L}_{\text{REG}}, \quad (9)$$

where \mathcal{L}_{REC} is the reconstruction loss $\|x - D(C(x))\|_2^2$, $\mathcal{L}_{\text{C}}^{\text{RAE}}$ the regularizer for the code space ($\frac{1}{2}\|c\|^2$), and \mathcal{L}_{REG} is the explicit regularizer for the decoder parameter space ($\|\theta_D\|_2^2$ in our case).

We then obtain the feature encoding $C(\cdot)$ as the encoder of the RAE. In this case, d is the dimension of the

auto-encoder bottleneck. Finally, we fit the generative foreground model p_F , using either a single Gaussian or a mixture of Gaussians, i.e., we adopt the idea first proposed in [16], to obtain a regularized auto-encoder (RAE). However, in order to use the RAE in the context of trajectory optimization, we also fit a background model, by using the same encoder $C(\cdot)$ and imputing a different density p_B .

4.2. Probabilistic Principal Component Analysis

A well known classical generative modeling technique is the Probabilistic Principal Component Analysis (PPCA) model by Tipping and Bishop [41]. In PPCA, we assume that the data follows a linear factor analysis distribution,

$$x = Wc + \mu + \epsilon, \quad (10)$$

where x is the observation, c a latent code vector, and W is a $d \times q$ matrix describing how the observation and latent variables relate. The mean μ allows the model to have non-zero mean and $\epsilon \sim \mathcal{N}(0, \sigma^2 I)$ is zero-mean Gaussian noise with covariance $\sigma^2 I$.

The maximum likelihood estimates (MLE) of W can be obtained in closed form using SVD [41]:

$$W_{ML} = U_q(\Lambda_q - \sigma^2 I)^{1/2} R, \quad (11)$$

and the MLE of σ , $\sigma_{ML}^2 = \frac{1}{d-q} \sum_{j=q+1}^d \lambda_j$, where the q columns of U_q are principal eigenvectors of S and their corresponding eigenvalues in Λ_q . Above R is an arbitrary $q \times q$ rotation matrix, and $\lambda_{q+1}, \dots, \lambda_d$ are the eigenvalues ‘‘lost’’ in W_{ML} . Conversely, we have a density of c over x :

$$P(c|x) \sim \mathcal{N}(M^{-1}W^T(x - \mu), \sigma^2 M^{-1}) \quad (12)$$

where $M = W^T W + \sigma^2 I$, which we can use to obtain an estimate for c given a measured x .

4.3. Random Projection Features

Since random projections preserve data statistics with a high probability [44], we can also use a random projection as a feature encoder. In particular, let A be an $n \times k$ random matrix whose entries are independently sampled from $\mathcal{N}(0, 1)$. For any arbitrary data vector $x \in \mathbb{R}^n$ the random projection $C(x)$ defined as

$$c \doteq C(x) = \frac{1}{\sqrt{k}} A^T x \quad (13)$$

preserves distance in the original feature space.

Indeed, by Lemma 1.3 in [44] we have

$$\mathbf{E}(\|c\|^2) = \|x\|^2 \quad (14)$$

$$P(\|c\|^2 - \|x\|^2 \geq \eta \|x\|^2) < 2e^{-(\eta^2 - \eta^3)k/4} \quad (15)$$

for any $\eta > 0$. Thus when k is sufficiently large, we can expect that the random project will preserve the L_2 distance of

vectors with a high probability. Consequently, we can use the random projection above as an encoder, under the assumption that densities fitted to this lower-dimensional feature space will model densities in the original image space. Because this encoding C is *not* learned, unlike RAE and PPCA, it provides a good baseline model.

4.4. Big Transfer

In addition to feature encodings, we also experiment with image classification to directly infer the probability of a given image patch being a foreground p_F or background p_B image. We evaluate Big Transfer [26] in our results which is outlined below.

Big Transfer (BiT) is a training paradigm that leverages a pre-trained and modified ResNet-v2 [19] architecture along with data-specific training parameters that have achieved state-of-the-art results on a series of downstream tasks [26]. In particular, all Batch Normalization [21] layers in the ResNet model are replaced with Group Normalization [47] layers and all convolutional layers implement Weight Standardization [35]. The BiT-M model, which we experiment with, is then trained on the ImageNet-21k [13] dataset and is provided for training on downstream classification tasks.

To obtain our foreground and background classifier, we fine-tune the BiT-M model using the BiT-Hyperrule recommended learning rate schedule, resolution, and MixUp regularization [49] on the downstream foreground and background bee hive image patches. This ResNet-v2 model with a softmax classification head then directly infers the probability p of new image patches in our dataset being foreground p_F or background p_B images.

5. Results

We evaluated our method on a challenging social insect dataset consisting of video of hundreds of bees moving over a bee hive grating, made public by OIST [6]. In this case the space of poses G is the Lie group $SE(2)$ of 2D Euclidean rigid transforms, and the differentiable warp R extracts an oriented bounding box centered on the pose $g_k \doteq (x_k, y_k, \theta_k)$. We iteratively optimize the factor graph at each time x_k to recover the state z_k on a set of eighty frames for each of twenty labeled bee tracks.

5.1. Dataset and Evaluation Metrics

The OIST dataset contains a set of bee annotations that have been hand labelled over hundreds of frames from a video of the bee hive shown in Figure 4. Each video frame has a resolution of 2560×2560 with 70×40 labeled bounding boxes. For training, the feature encoding $C(\cdot)$ is trained through reconstructing the region R enclosed within an oriented bounding box for a given pose g_k for the RAE, RP, and PPCA models. For the BiT approach, the model is trained to directly infer the probability that a given image

patch is foreground p_F or background p_B . These models are trained on 3,000 foreground and 3,000 background bee images present within the first 100 frames of the dataset. The image patches are then evaluated on a hold-out test set of 20 tracking sequences each with eighty frames.

We report tracking performance as the Expected Average Overlap (EAO), which is a function of the accuracy and robustness of a tracker over all tracking sequences in a dataset [43]. We also show the average accuracy and robustness over all sequences as individual metrics, where accuracy is defined as the average overlap between the predicted and ground truth oriented bounding boxes before failure, and robustness is the proportion of frames where the tracker has succeeded in tracking the correct object. These metrics are calculated over eighty frames used for tracking in the hold-out test dataset.

5.2. Implementation Details

We first train a feature encoding $C(\cdot)$ on the oriented bounding boxes centered on each pose g_k for all labelled insects in the first one hundred frames. For the RP, PPCA, and RAE models, we then fit a foreground model p_F and background model p_B to create the foreground factor ϕ_F and background factor ϕ_B trained on these poses. We found that modeling both p_F and p_B as multivariate Gaussian generative models obtained the best results. With BiT we use the softmax output to directly infer the probability of an image patch being foreground p_F or background p_B . To infer the MAP trajectory Z^* on a given sequence, we iteratively add measurements for each frame at time t_k to a factor graph as shown in Figure 2 and optimize to recover the hidden state z_k of the object across the track. This inference is conducted across eighty frames for all twenty tracks to obtain the MAP trajectory Z^* across all sequences in the test dataset.

We evaluated Random Projection (RP), Probabilistic Principal Component Analysis (PPCA), Regularized Auto-encoder (RAE), and Big Transfer (BiT) models to determine their performance in imputing a useful set of densities p_F and p_B for the factor graph to optimize on. The RAE model is constructed with a single convolution and max pool layer layer followed by two fully connected layers which are then up-sampled in an equivalent inverse decoder step. The auto-encoder is penalized using reconstruction loss on the foreground image patches and trained using the Adam [25] optimizer with a learning rate of 0.001. Each auto-encoder is trained outside of the factor graph optimization loop and the trained weights are loaded in for image patch encoding when the deep factors are initialized. The BiT training process follows the procedures outlined in BiT-Hyperrule [26] for the BiT-M model pre-trained on ImageNet-21k.

The entire trajectory optimization pipeline is implemented with Swift for TensorFlow (S4TF, see [36]), al-

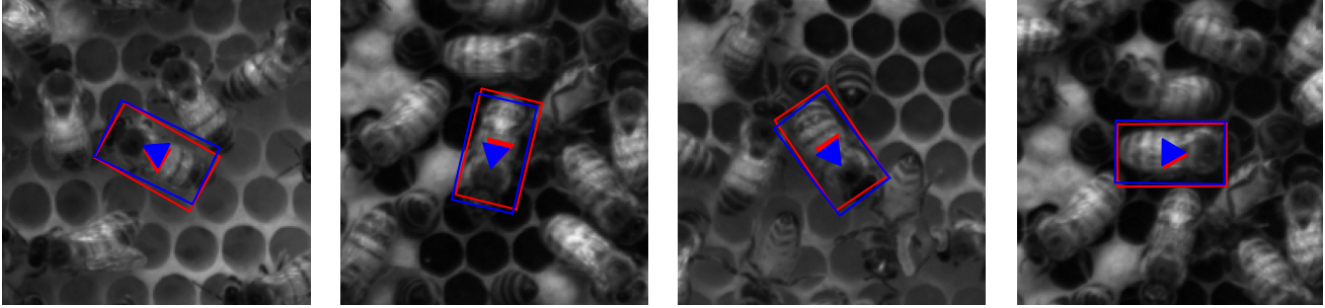


Figure 4. Sample beehive images from OIST dataset from four of the twenty distinct tracks. Shown on each image are the bounding boxes oriented by the 2D pose of the bee, where the blue bounding box is the ground truth and the red bounding box is the corresponding prediction from our algorithm.

lowing for a simple implementation of auto-differentiation across the entire factor graph optimization process.

5.3. Deep Features Outperform Linear Features

In the first set of results, we show that using deep factors from BiT and RAE models outperform both a linear PPCA appearance model [24] and a linear feature set obtained using random projections (RP, see [44]). We also show that the RAE models with a higher number of output features achieve higher EAO than their counterparts with fewer dimensions. Furthermore, we find that the BiT approach yields higher tracking accuracy whereas the RAE 256 model achieves greater robustness.

To determine the efficacy of deep factors, we ran a series of experiments to find the EAO performance of RP, PPCA, and RAE models each with bottleneck sizes $d \in \{16, 64, 256\}$ alongside the BiT approach and found that the BiT and RAE 256 approaches outperformed every other factor graph configuration as seen in Figure 5. The RAE model with bottleneck size $d = 256$ outperformed the linear feature encodings with 0.75 accuracy and 0.98 robustness while the BiT approach achieved the highest accuracy 0.78 with comparable robustness 0.95 to the RAE 256 approach. The top end EAO scores for each model increase from 0.27 EAO for RP to 0.55 for PPCA to 0.75 for RAE. Across each output size, the RAE and BiT models achieved significantly better results, demonstrating the effectiveness of deep factors.

Another important finding is that increasing the bottleneck size d of the RAE model significantly increases EAO performance. As the bottleneck dimensionality d of the RAE increases from 16 to 256, performance significantly improves from 0.39 EAO score to 0.75. We also found that for bottleneck size above the 256 threshold $d > 256$, EAO performance stayed relatively constant. This demonstrates that increasing the complexity of the RAE model yields significant gains in its ability to find an effective feature encoding $C(\cdot)$ that efficiently condenses high dimensional inputs, resulting in increased EAO for these larger bottleneck di-

mensions $d \geq 256$.

5.4. Deep Factors Outperform Deep Trackers

The RAE 256 and BiT deep factor graph approaches obtained higher EAO, accuracy, and robustness than SiamMask, a state-of-the-art short-term object tracker, across all test sequences. SiamMask [46] is a representative of a family of Siamese trackers that can produce oriented bounding boxes by estimating a minimal area rectangle around a segmentation mask [31, 50, 48].

We evaluated the performance of SiamMask using a model trained solely on VOT2019 as well as the same model fine-tuned on the OIST dataset. SiamMask comes with models pre-trained on either VOT2019 [27] or DAVIS2016 [34] datasets and the VOT2019 model is slightly better performing on the OIST testing dataset. SiamMask takes a single-bounding box at initialization, producing oriented bounding boxes and object segmentation masks. SiamMask is made up of an offline-trained fully-convolutional Siamese network [2]. At inference, a larger $255 \times 255 \times 3$ search image from the current frame and a smaller $127 \times 127 \times 3$ target image from the initial frame are both passed into the same CNN. This yields two dense feature maps which are depth-wise cross-correlated. The result is a response map which will indicate where in the search image the object is most likely located.

In Figure 5 we show that the the RAE 256 and BiT trackers outperform both SiamMask and SiamMask fine-tuned on the OIST dataset. The RAE tracker achieves higher accuracy and robustness than the better performing fine-tuned SiamMask model, increasing accuracy from 0.69 to 0.75 and robustness from 0.76 to 0.98. Similarly, the BiT approach improves accuracy from 0.69 to 0.78 and robustness from 0.76 to 0.95. Because of the nature of this dataset there are multiple similar looking objects in each frame. SiamMask’s Siamese network will yield a high response value to objects that look very similar to the target object which appear close to the target location in the frame. This can cause the tracker’s prediction to jump to nearby bees

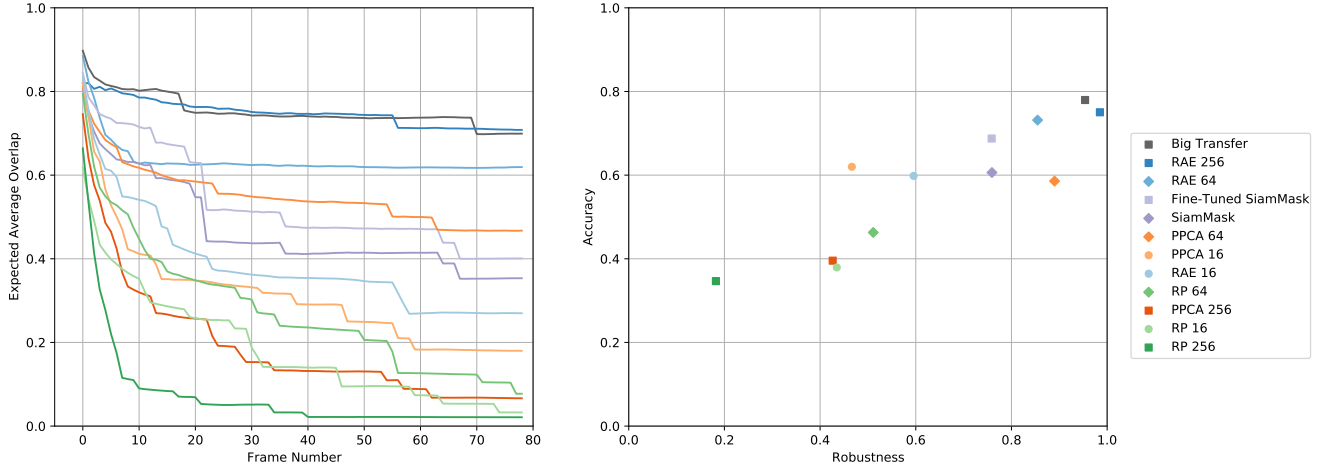


Figure 5. Performance of the BiT [26], RAE, PPCA, RP Factor Graphs alongside the state-of-the-art model SiamMask [46] on the test dataset. The EAO curve for each model (left) and the AR-plot (right) are calculated over all twenty object tracking sequences for eighty frames. Each factor graph configuration is listed by its appearance encoder and the dimensionality of the encoded output $d \in \{16, 64, 256\}$.

	d	Accuracy	Robustness	EAO
BiT	BiT-M	0.78	0.95	0.75
RAE	256	0.75	0.98	0.75
	64	0.73	0.85	0.63
	16	0.60	0.60	0.39
PPCA	256	0.40	0.43	0.19
	64	0.59	0.89	0.55
	16	0.62	0.47	0.31
RP	256	0.35	0.18	0.07
	64	0.46	0.51	0.27
	16	0.38	0.43	0.18

Table 1. The accuracy and robustness of the feature encoding $C(\cdot)$ configurations from our experimental results with encoding output dimensionality $d \in \{16, 64, 256\}$. For consistency, all models leveraged multivariate Gaussian models for both the foreground p_F and background p_B generative densities. The BiT model implements the default BiT-M ResNet-v2 model architecture [26].

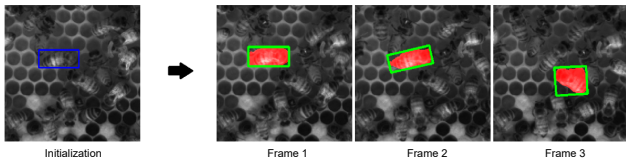


Figure 6. SiamMask fails to keep track of the correct bee and jumps to an adjacent bee. Bounding box initialization (left). Output segmentation masks and oriented bounding boxes of the next three frames (right).

due to the very crowded environment of a beehive, reducing the robustness of that sequence.

The fine-tuned SiamMask model outperformed the model trained solely on the VOT dataset, increasing accuracy from 0.61 to 0.68. The robustness, however, re-

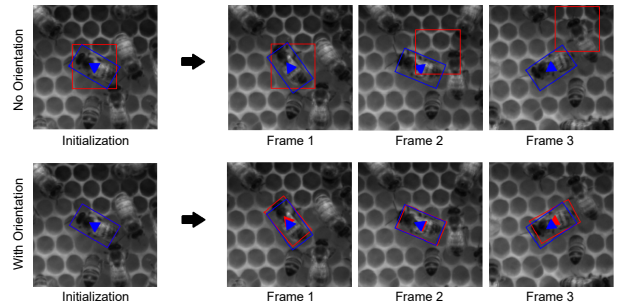


Figure 7. RAE 256 factor graph trained with a differentiable bounding box (top) and an differentiable oriented bounding box (bottom) where the prediction is shown in red and the ground truth in blue. Explicitly modeling the orientation through an oriented bounding box allows for the factor graph to correctly map the trajectory of the rotating bee, whereas by modeling just translation we see that as the most likely bounding box chosen was incorrect as the bee rotates.

mained constant at 0.76 despite the additional domain-specific training. The training data used for fine-tuning is comprised of the first one hundred frames of the OIST dataset as well as twenty tracks containing the oriented bounding box coordinates for twenty different bees. We converted the training data to match the input required for SiamMask training. Oriented bounding boxes were converted to segmentation masks by constructing oriented ellipses with the same center, angle, width, and height of the oriented bounding boxes.

5.5. Differentiable Oriented Bounding Boxes

Explicitly modeling orientation through an oriented bounding box performs better than modeling the orientation as part of the appearance variables a_k . Figure 7 shows

a situation where a RAE 256 model trained with an oriented differentiable bounding box outperforms a RAE 256 model with a bounding box that does not model orientation. We see that as the bee with appearance a_k rotates near another bee with similar appearance \hat{a}_k , the factor graph with the oriented bounding box is able to correctly reconstruct the trajectory Z^* while the bounding box without orientation fails by switching to the bee with appearance \hat{a}_k . The explicit orientation information at time t_k allows the factor graph to optimize with better constraints on the possible pose g_{k+1} of the bee in the next time step t_{k+1} ,

In general, the tracker that is able to optimize the explicit orientation of the bounding box attains higher robustness and accuracy across all sequences because of the additional orientation information. Using the RAE 256 model with oriented bounding boxes improves accuracy from 0.39 to 0.75 and robustness from 0.33 to 0.98 averaged across all tracks. Furthermore, when orientation is not captured, a 70×70 square bounding box must be used to ensure that the 40×70 bee will be encapsulated by the bounding box. This reduces the specificity of the of the object tracker which is also less desirable as it does not capture the exact location of the object. It also increases the complexity of the feature encoding $C(\cdot)$ by increasing the size of the input image patch. Overall, explicitly modeling the orientation through a differentiable oriented bounding box provides more consistent and precise results than attempting to capture orientation information through the appearance a_k .

5.6. Choice of Generative Model is Important

In this experiment, we establish that using a set of multivariate Gaussian generative densities for the foreground model p_F and background model p_B achieves higher EAO than using a multivariate Gaussian foreground model p_F and a naïve Bayes background model p_B with a RAE 256 feature encoding $C(\cdot)$. In this case, we consider a multivariate Gaussian model for the foreground density p_F and both a multivariate Gaussian model and a naïve Bayes model for the the background density p_B . We show that using a full covariance Gaussian for the background model increases accuracy by 0.31 and robustness by 0.72 as opposed to the naïve Bayes model when using the RAE 256 feature encoding $C(\cdot)$. Based on these results, it is clear that the full $d \times d$ covariance matrix in the multivariate Gaussian model is necessary to capture the relationship between features of the RAE 256 encoded background regions $C(R_B)$.

In Figure 8, we also illustrate that the foreground and background models p_F and p_B are not represented well by a mixture of Gaussian models in the two component plane output by t-SNE [42], indicating that a Gaussian mixture also would not represent the data well in the higher RAE 256 encoded dimension $d = 256$. We applied the RAE 256 feature encoding $C(\cdot)$ on six thousand foreground and back-

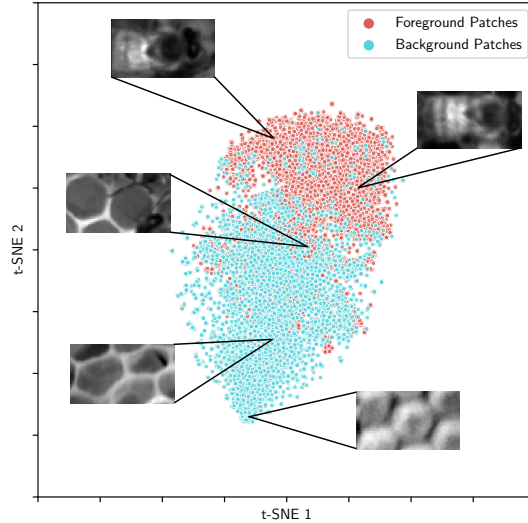


Figure 8. The two component t-SNE [42] visualization of the encoded image patches using the RAE 256 feature encoding $C(\cdot)$ for six thousand foreground and background images. Encoded features $C(R_F)$ and $C(R_B)$ have a strong grouping in the two t-SNE dimensions, indicating that a mixture of Gaussian models would not represent the data well in the higher encoded dimension $d = 256$. Furthermore, we validate the need to represent the encoded foreground and background regions with two separate generative densities p_F and p_B as they separate well in the two component t-SNE output. The majority of the overlap between the two encoded regions are those background regions R_B which do contain some part of a bee in the periphery of the image.

ground regions R and reduced the encoding dimensionality $d = 256$ to two $d = 2$ using t-SNE with perplexity 35. By analyzing the output from these two components, it is clear that within the foreground regions R_F and background regions R_B , there are no significantly separated groups that would imply the need for a mixture of Gaussian models. Alongside this finding, we also validate the necessity for splitting the encoded foreground regions $C(R_F)$ and encoded background regions $C(R_B)$ into separate generative densities p_F and p_B , as it is clear they do not exhibit the same encoded output from the RAE 256 model.

6. Conclusions

Using a deep feature encoding in conjunction with generative models over the features in a factor-graph based, probabilistic trajectory optimization framework yields excellent results in a challenging application. Our method leverages the Lie group properties of the tracked target’s pose by using a differentiable warp, which is optimized in a structured probabilistic optimization framework.

This can form the basis for more complicated applications. Above we experimented with $SE(2)$, and it would be of interest to see the results for more general poses, e.g., 2D

similarity transforms and full 3D poses, similar to [30].

While we obtain good results using the auto-encoder features, the RAE is trained for image reconstruction rather than performance on the trajectory optimization task. Training the auto-encoder with the final task, i.e., with the optimization in the loop, is the subject of future work. Finally, while our current approach uses a supervised, off-line training method, but nothing prevents on-line adaptation of either features and the generative foreground model.

References

- [1] D. Belanger and A. McCallum. Structured Prediction Energy Networks. In M. F. Balcan and K. Q. Weinberger, editors, *Proceedings of The 33rd International Conference on Machine Learning*, volume 48 of *Proceedings of Machine Learning Research*, pages 983–992, New York, New York, USA, 20–22 Jun 2016. PMLR. 2
- [2] L. Bertinetto, J. Valmadre, J. F. Henriques, A. Vedaldi, and P. H. S. Torr. Fully-Convolutional Siamese Networks for Object Tracking. In G. Hua and H. Jégou, editors, *Computer Vision – ECCV 2016 Workshops*, pages 850–865, Cham, 2016. Springer International Publishing. 2, 6
- [3] G. Bhat, M. Danelljan, L. V. Gool, and R. Timofte. Learning Discriminative Model Prediction for Tracking. In *Int. Conf. Comput. Vis.*, pages 6181–6190. IEEE, 2019. 2
- [4] D. S. Bolme, J. Ross, B. Bruce, A. Draper, and Y. M. Lui. Visual object tracking using adaptive correlation filters. In *IEEE Conf. Comput. Vis. Pattern Recog.*, pages 2544–2550, 2010. 2
- [5] K. Bozek, L. Hebert, A. S. Mikheyev, and G. J. Stephens. Towards Dense Object Tracking in a 2D Honeybee Hive. In *2018 IEEE/CVF Conference on Computer Vision and Pattern Recognition*, pages 4185–4193, 2018. 2
- [6] K. Bozek, L. Hebert, Y. Portugal, and G. J. Stephens. Markerless tracking of an entire insect colony. *bioRxiv*, 2020. 5
- [7] J. Carreira, P. Agrawal, K. Fragkiadaki, and J. Malik. Human Pose Estimation with Iterative Error Feedback. In *IEEE Conf. Comput. Vis. Pattern Recog.*, pages 4733–4742, 2016. 2
- [8] B. Chen, D. Wang, P. Li, S. Wang, and H. Lu. Real-Time ‘Actor-Critic’ Tracking. In V. Ferrari, M. Hebert, C. Sminchisescu, and Y. Weiss, editors, *Computer Vision – ECCV 2018*, pages 328–345, Cham, 2018. Springer International Publishing. 1
- [9] X. Chen, B. Yan, J. Zhu, D. Wang, X. Yang, and H. Lu. Transformer Tracking. In *IEEE Conf. Comput. Vis. Pattern Recog.*, pages 8126–8135, June 2021. 1
- [10] R. Clark, S. Wang, H. Wen, A. Markham, and N. Trigoni. VINet: Visual-Inertial Odometry as a Sequence-to-Sequence Learning Problem. In *AAAI*, 2017. 2
- [11] J. Czarnowski, T. Laidlow, R. Clark, and A. J. Davison. DeepFactors: Real-Time Probabilistic Dense Monocular SLAM. *IEEE Robotics and Automation Letters*, 5(2):721–728, 2020. 2
- [12] M. Danelljan, G. Häger, F. S. Khan, and M. Felsberg. Learning Spatially Regularized Correlation Filters for Visual Tracking. In *Int. Conf. Comput. Vis.*, pages 4310–4318, 2015. 2
- [13] J. Deng, W. Dong, R. Socher, L. Li, K. Li, and L. Fei-Fei. ImageNet: A large-scale hierarchical image database. In *IEEE Conf. Comput. Vis. Pattern Recog.*, pages 248–255, 2009. 5
- [14] J. Dong, M. Mukadam, F. Dellaert, and B. Boots. Motion Planning as Probabilistic Inference using Gaussian Processes and Factor Graphs. In *Robotics: Science and Systems (RSS)*, 2016. 2
- [15] H. Fan. *Algorithms and Benchmarks for Robust Visual Object Tracking*. PhD thesis, State University of New York at Stony Brook, 2021. 2
- [16] P. Ghosh, M. Sajjadi, A. Vergari, M. Black, and B. Scholkopf. From Variational to Deterministic Autoencoders. In *Int. Conf. Learn. Represent.*, 2020. 4
- [17] I. Goodfellow, J. Shlens, and C. Szegedy. Explaining and Harnessing Adversarial Examples. In *International Conference on Learning Representations*, 2015. 2
- [18] R. Hartley, M.G. Jadidi, L. Gan, J. Huang, J.W. Grizzle, and R.M. Eustice. Hybrid Contact Preintegration for Visual-Inertial-Contact State Estimation Using Factor Graphs. In *2018 IEEE/RSJ International Conference on Intelligent Robots and Systems (IROS)*, pages 3783–3790. IEEE, 2018. 2
- [19] K. He, X. Zhang, S. Ren, and J. Sun. Identity Mappings in Deep Residual Networks. *ECCV*, pages 630–645, 2016. 5
- [20] J. F. Henriques, R. Caseiro, P. Martins, and J. Batista. High-Speed Tracking with Kernelized Correlation Filters. *IEEE Transactions on Pattern Analysis and Machine Intelligence*, 37(3):583–596, 2015. 2
- [21] S. Ioffe and C. Szegedy. Batch normalization: Accelerating deep network training by reducing internal covariate shift. In *International conference on machine learning*, pages 448–456. PMLR, 2015. 5
- [22] M. Jaderberg, K. Simonyan, A. Zisserman, et al. Spatial transformer networks. In *Adv. Neural Inform. Process. Syst.*, pages 2017–2025, 2015. 2
- [23] B. Jung and G. S. Sukhatme. Real-time Motion Tracking from a Mobile Robot. *International Journal of Social Robotics*, 2(1):63–78, Mar. 2010. 1
- [24] Z. Khan, T. Balch, and F. Dellaert. A Rao-Blackwellized Particle Filter for EigenTracking. In *IEEE Conf. Comput. Vis. Pattern Recog.*, volume 2, pages 980–986, 2004. 2, 6
- [25] Diederik P Kingma and Jimmy Ba. Adam: A method for stochastic optimization. *arXiv preprint arXiv:1412.6980*, 2014. 5
- [26] A. Kolesnikov, L. Beyer, X. Zhai, J. Puigcerver, J. Yung, S. Gelly, and N. Houlsby. Big Transfer (BiT): General Visual Representation Learning. *ECCV*, pages 491–507, 2020. 4, 5, 7
- [27] M. Kristan, J. Matas, A. Leonardis, M. Felsberg, R. Pflugfelder, J.-K. Kamarainen, L. Č. Zajc, O. Drbohlav, A. Lukežič, A. Berg, A. Eldesokey, J. Kapyla, and G. Fernandez. The Seventh Visual Object Tracking VOT2019 Challenge Results, 2019. 6
- [28] Y. LeCun, S. Chopra, R. Hadsell, F. J. Huang, and et al. A tutorial on energy-based learning. In *PREDICTING STRUCTURED DATA*. MIT Press, 2006. 2

- [29] Bo Li, Junjie Yan, Wei Wu, Zheng Zhu, and Xiaolin Hu. High performance visual tracking with siamese region proposal network. In *2018 IEEE/CVF Conference on Computer Vision and Pattern Recognition*, pages 8971–8980, 2018. [3](#)
- [30] Z. Lv, F. Dellaert, J. Rehg, and A. Geiger. Taking a Deeper Look at the Inverse Compositional Algorithm. In *IEEE Conf. Comput. Vis. Pattern Recog.*, 2019. [2](#), [9](#)
- [31] Z. Ma, L. Wang, H. Zhang, W. Lu, and J. Yin. RPT: Learning Point Set Representation for Siamese Visual Tracking, 2020. [1](#), [6](#)
- [32] S. M. Marvasti-Zadeh, L. Cheng, H. Ghanei-Yakhdan, and S. Kasaei. Deep Learning for Visual Tracking: A Comprehensive Survey. *IEEE Transactions on Intelligent Transportation Systems*, pages 1–26, 2021. [1](#)
- [33] A. Mathis, P. Mamidanna, K. M. Cury, T. Abe, V. N. Murthy, M. Mathis, and M. Bethge. DeepLabCut: markerless pose estimation of user-defined body parts with deep learning. *Nature Neuroscience*, 21:1281–1289, 2018. [2](#), [3](#)
- [34] F. Perazzi, J. Pont-Tuset, B. McWilliams, L. Van Gool, M. Gross, and A. Sorkine-Hornung. A Benchmark Dataset and Evaluation Methodology for Video Object Segmentation. In *Computer Vision and Pattern Recognition*, 2016. [6](#)
- [35] S. Qiao, H. Wang, C. Liu, W. Shen, and A. Yuille. Micro-Batch Training with Batch-Channel Normalization and Weight Standardization, 2020. [5](#)
- [36] B. Saeta and D. Shabalin. Swift for TensorFlow: A portable, flexible platform for deep learning. *Proceedings of Machine Learning and Systems*, 3, 2021. [5](#)
- [37] S. Schönborn, B. Egger, A. Forster, and T. Vetter. Background modeling for generative image models. *Computer Vision and Image Understanding*, 136:117–127, 2015. [3](#)
- [38] P. Sodhi, E. Dexheimer, M. Mukadam, S. Anderson, and M. Kaess. LEO: Learning Energy-based Models in Factor Graph Optimization. In *5th Annual Conference on Robot Learning*, 2021. [2](#)
- [39] R. Tao, E. Gavves, and A. W. M. Smeulders. Siamese instance search for tracking. In *Proceedings of the IEEE conference on computer vision and pattern recognition*, pages 1420–1429, 2016. [2](#)
- [40] P. V. Teixeira, M. Kaess, F. S. Hover, and J. J. Leonard. Underwater Inspection using Sonar-based Volumetric Submaps. In *IEEE/RSJ Intl. Conf. on Intelligent Robots and Systems (IROS)*, pages 4288–4295, Daejeon, Korea, Oct. 2016. [2](#)
- [41] M.E. Tipping and C.M. Bishop. Probabilistic principal component analysis. *Journal of the Royal Statistical Society, Series B* 61(3):611–622, 1999. [4](#)
- [42] L. van der Maaten and G. Hinton. Visualizing Data using t-SNE. *Journal of Machine Learning Research*, 9(86):2579–2605, 2008. [8](#)
- [43] L. Č. Zajc, A. Leonardis, and M. Kristan. Visual object tracking performance measures revisited, Apr 2016. [5](#)
- [44] S. S. Vempala. *The Random Projection Method*, volume 65. American Mathematical Society, 2005. [4](#), [6](#)
- [45] C. Wang, H. K. Galoogahi, C. H. Lin, and S. Lucey. DeepLK for Efficient Adaptive Object Tracking. In *2018 IEEE International Conference on Robotics and Automation (ICRA)*, pages 627–634, 2018. [2](#)
- [46] Q. Wang, L. Zhang, L. Bertinetto, W. Hu, and P. H. S. Torr. Fast Online Object Tracking and Segmentation: A Unifying Approach. In *IEEE Conf. Comput. Vis. Pattern Recog.*, pages 1328–1338, 2019. [2](#), [3](#), [6](#), [7](#)
- [47] Y. Wu and K. He. Group normalization. In *Proceedings of the European conference on computer vision (ECCV)*, pages 3–19, 2018. [5](#)
- [48] B. Yan, X. Zhang, D. Wang, H. Lu, and X. Yang. Alpha-refine: Boosting tracking performance by precise bounding box estimation. In *Proceedings of the IEEE/CVF Conference on Computer Vision and Pattern Recognition*, pages 5289–5298, 2021. [6](#)
- [49] H. Zhang, M. Cisse, Y. N. Dauphin, and D. Lopez-Paz. mixup: Beyond Empirical Risk Minimization. *Intl. Conf. on Learning Representations*, 2018. [5](#)
- [50] Z. Zhang, Y. Liu, B. Li, W. Hu, and H. Peng. Toward Accurate Pixelwise Object Tracking via Attention Retrieval. *IEEE Transactions on Image Processing*, 30:8553–8566, 2021. [6](#)
- [51] Z. Zhang, H. Peng, J. Fu, B. Li, and W. Hu. Ocean: Object-aware anchor-free tracking. *ECCV*, pages 771–787, 2020. [2](#)
- [52] B. Zhong, B. Bai, J. Li, Y. Zhang, and Y. Fu. Hierarchical Tracking by Reinforcement Learning-Based Searching and Coarse-to-Fine Verifying. *IEEE Transactions on Image Processing*, 28(5):2331–2341, 2019. [1](#)